INTERNATIONAL JOURNAL OF ROBUST AND NONLINEAR CONTROL
Int. J. Robust Nonlinear Control 2001; **11**:1023–1042 (DOI: 10.1002/rnc.643)

Inherent limitations and control design for camless engine idle speed dynamics

Yan Wang[1], Anna Stefanopoulou[2,*,†] and Roy Smith[3]

[1]*Mechanical & Environmental Engineering Department, University of California, Santa Barbara, CA 93106, U.S.A.*
[2]*Mechanical Engineering Department, University of Michigan, Ann Arbor, MI 48109, U.S.A.*
[3]*Electrical & Computer Engineering Department, University of California, Santa Barbara, CA 93106, U.S.A.*

SUMMARY

The idle speed control problem of a spark-ignited engine equipped with a camless valvetrain is considered. The camless valvetrain allows control of the individual intake and exhaust valves of each cylinder and can be used to achieve unthrottled operation, and consequently, optimize the engine performance. We formulate the speed control problem for this engine and show that it exhibits unstable open-loop behaviour with a significant delay in the feedback loop. The instability is intrinsic to the unthrottled operation and specific to the camless actuation used to achieve the unthrottled operation. The delay is caused by the discrete combustion process and the sensor/computer/actuator interface. We demonstrate the inherent system limitations associated with the unstable dynamics and the delay and provide insight on the structural (plant) design that can alleviate these limitations. Finally, stabilizing controllers using classical and modern robust design techniques are presented and tested on a nonlinear simulation model. Copyright © 2001 John Wiley & Sons, Ltd.

KEY WORDS: engine control; robust control; stability; linearization

1. INTRODUCTION

In this paper we study the idle speed control problem of an unthrottled spark ignition engine equipped with an electro-hydraulic camless and springless valvetrain. In contrast to the majority of conventional automotive engines that operate with a valve motion fixed to the crankshaft rotation through the mechanical link of the camshaft, the camless valvetrain system allows fully controlled valve events. Although the conventional system has proven to be convenient and safe, its fixed valve timing is necessarily a compromise of combustion stability, fuel economy and maximum torque objectives. The camless valvetrain, on the other hand, allows the optimization

---

* Correspondence to: Anna Stefanopoulou, Mechanical Engineering Department, University of Michigan, G058 Lay Auto Lab, 1231, Beal Ave., Ann Arbor, MI 48109-2121, U.S.A.
†E-mail: annastef@umich.edu

Contract/grant sponsor: National Science Foundation; contract/grant numbers: ECS-00-49025 and ECS-99-78562

of the exhaust and intake valve timing, motion and activation for individual cylinder gas exchange control.

Various studies have shown that a camless valvetrain can alleviate many engine design tradeoffs by supplying extra degrees of freedom to the overall powertrain system [1–3]. In particular, it has been shown that controlling the intake valve events can eliminate the need for throttled operation in gasoline engines and thus obtain fuel economy benefits [4–6]. In conventional gasoline engines, the largest amount of throttling corresponds to the idle speed mode. It follows that unthrottled camless operation will result in significant fuel saving if applied to idle operation. Hence, one of the critical steps in obtaining the projected steady-state benefits of camless technology is the design of an idle speed controller for this innovative engine configuration.

To this end, we first analyse the open-loop dynamics pertinent to the camless unthrottled operation. It is then demonstrated that the speed regulation problem in a camless engine is more challenging than the idle speed control (ISC) problem for conventional throttled operation. Specifically, the dynamic behaviour of the camless engine speed is open-loop unstable. Indeed, the camless engine would exhibit unbounded speed drop due to a bounded (even infinitesimally small) torque disturbance, if it were not for the physical minimum engine speed saturation (stall) limit. In comparison, a conventional throttled engine exhibits a bounded speed drop for a bounded sufficiently small torque disturbance and it is open-loop stable. Depending on the magnitude of the torque disturbance, the resulting speed drop can still cause engine stall. In both cases a closed-loop controller is necessary to improve transient performance and ensure disturbance rejection. In the case of the camless engine, however, the controller needs to stabilize the speed dynamics in addition to the other two control tasks. The structural source and the implications of the instability for the control design is an important aspect in the development of camless engines. We show that the instability is intrinsic to the unthrottled operation and specific to the camless actuation used to achieve the unthrottled operation. It is, indeed, well known in the automotive community that 'stable' unthrottled engine operation is difficult to achieve during low load, and in particular, during idle conditions [7, 8]. With this work we substantiate this observation and develop the necessary framework to analyse and control the process. Furthermore, we use system theoretical tools to obtain the limits of achievable performance. These fundamental limits are consequently used in designing and evaluating robust controllers of different complexity. Our analysis and control design is based on a mean-value model.

2. ROTATIONAL DYNAMICS

The objective of ISC is to maintain constant (and low) engine speed during the application of load. For a comprehensive review of ISC see Reference [9]. In an ISC problem, the commonly chosen control variable is the throttle angle (or air bypass valve position). Sometimes, the spark timing and the air/fuel ratio are also chosen, but in most cases, these actuators are reserved for other engine control functions. One of the idle speed control design difficulties, common to all spark ignition port fuel injection engines, arises from the variable induction-to-power delay and the actuator authority which imposes a fundamental limitation to the closed-loop bandwidth and restricts the disturbance rejection ability of the idle speed controller. Good fuel economy and emissions require low idle speed which aggravates the above difficulties because it results in a longer delay, and therefore, it imposes more strict limitations on the closed-loop bandwidth.

Moreover, low speed induces noise and combustion instability. To make things worse, the driver's perception of noise, vibration and harshness (NVH) characteristics is more acute during idle conditions making smooth idle speed operation a major driver concern.

In the unthrottled camless engine we utilize the intake valve duration for cylinder air flow regulation instead of the throttle or the air by-pass valve. Frequently in our camless ISC analysis we draw comparisons with the air by-pass valve control of a conventional throttled engine to highlight their differences. Figure 1 shows the block diagram of the unthrottled camless and the throttled conventional engines indicating their similarities and differences. Specifically, the rotational dynamics, net engine torque, torque due to friction and other losses, induction-to-power delay (I–P delay) and the cycle flow integration blocks are structurally similar for the two engines, while the breathing dynamics and the actuation dynamics are different.

A lumped parameter model can be used to describe the rotational dynamics that govern the engine speed $N(t)$ (rpm):

$$J\frac{60}{2\pi}\frac{\mathrm{d}N(t)}{\mathrm{d}t} = T_{qe}(t) - T_{qf}(t) - T_{qd}(t) - T_{ql}(t) \tag{1}$$

where J (kg m^2) is the total rotational inertia, T_{qe} (N m) the net engine generated torque, T_{qf} (N m) the torque due to mechanical friction and other losses, T_{qd} (N m) the disturbance torque and T_{ql} (N m) the load torque. The torque load, T_{ql}, during idle accounts for all the accessory steady-state loads, such as the cabin heater, rear window defroster, power steering, brake booster, etc. The disturbance load, T_{qd}, corresponds to the torque introduced due to abrupt changes in the

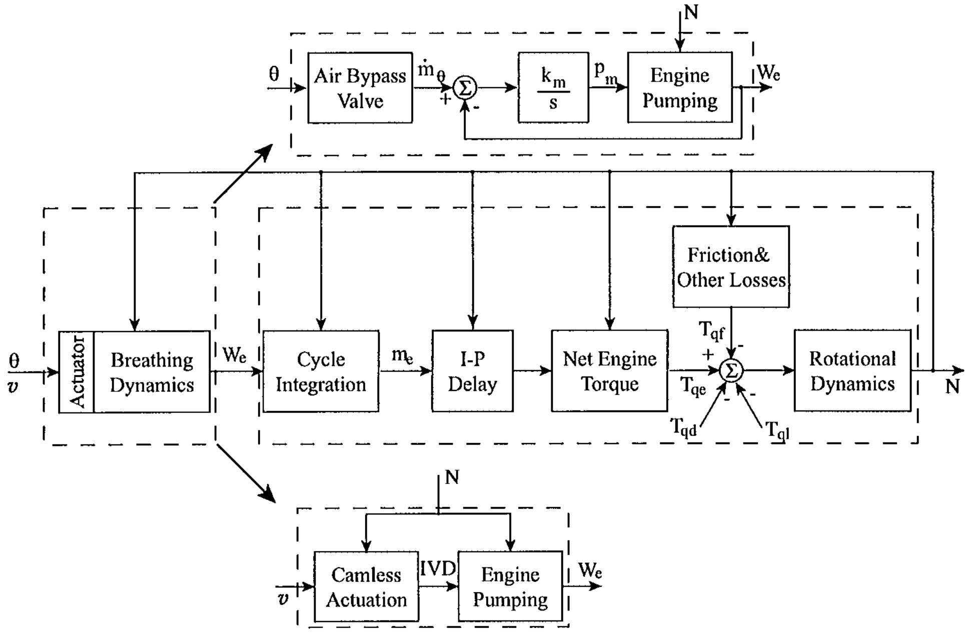

Figure 1. Block diagram of the camless unthrottled and the conventional throttled engines.

accessory load, In the worst case scenario, the torque load (all accessories) is as high as 50 N m and a typical disturbance load can be 15 N m.

To improve fuel efficiency, the camless actuation torque loss matches the valvetrain friction torque loss. The preliminary data from a prototype system shows, however, that the benefit from the unthrottled operation (significant reduction of pumping loss) is spent by the electrical load of the experimental actuator, and therefore, the camless net engine torque equation is similar to that of the conventional (even in absolute value). The net engine and friction torque are determined using experimental data for constant air-to-fuel ratio, Maximum brake torque (MBT) spark timing and zero exhaust gas recirculation:

$$T_{q\mathrm{f}}(t) = F_{T_{q\mathrm{f}}}(N(t)) \tag{2}$$

$$T_{q\mathrm{e}}(t) = F_{T_{q\mathrm{e}}}(m_\mathrm{e}(t-\tau_\mathrm{e}), N(t)) \tag{3}$$

where m_e (kg) is the engine air charge and τ_e (s) the I–P delay between the mass charge formation and the torque generation. The delay is constant in the crank-angle domain and, therefore, it is a function of the engine speed (N): $\tau_\mathrm{e} = 2\Delta T$, where $\Delta T = 120/nN$ (s) is the stroke event, and $n = 4$ for a 4-stroke engine, and therefore, $\Delta T = 30/N$.

In the presence of a torque disturbance ($T_{q\mathrm{d}}$ in (1)), the ISC task is to adjust the engine air charge (m_e) and generate the necessary engine torque ($T_{q\mathrm{e}}$) to maintain constant engine speed (N). The engine air charge is the integration of the instantaneous engine flow $\dot{m}_\mathrm{e}(t)$ (kg/s) during an engine cycle, that is $m_\mathrm{e} = \int_0^{4\Delta T} \dot{m}_\mathrm{e}(t)\,\mathrm{d}t$. By assuming a cycle-averaged uniform in time engine air flow W_e we obtain

$$m_\mathrm{e} = F_{m_\mathrm{e}}(W_\mathrm{e}, N) = W_\mathrm{e}\frac{120}{N} \tag{4}$$

It is interesting to analyse the stability of the idle speed regulation based on controlling the engine air charge (kg/cycle) versus controlling the averaged air flow (kg/s). One should expect considerably different dynamics since the transformation between the two inputs is not linear. It involves a feedback loop through the variable $4\Delta T = 120/N$ that depends on engine speed. We show in Section 5 that the linearized $\Delta m_\mathrm{e} \to \Delta N$ dynamics of both camless and conventional engines are stable with a pole close to the imaginary axis ('barely stable'). The linearized $\Delta W_\mathrm{e} \to \Delta N$ dynamics, however, are 'very stable' with a pole sufficiently far from the imaginary axis. Note that this analysis is also pertinent to diesel engines because the fuel control design can be based on fuel flow (kg/s) or fuel charge (kg/cycle) for a desired air-to-fuel ratio. Indeed, Guzzella *et al.* [10] show that the $\Delta m_\mathrm{e} \to \Delta N$ dynamics in a diesel engine are unstable because at low speeds the torque loss associated with friction and pumping increases slower than the indicated engine torque when speed increases. Note also that the diesel engine and the unthrottled camless engine have similarly small torque loss due to pumping. In the camless engine under investigation, however, the $\Delta m_\mathrm{e} \to \Delta N$ dynamics remain stable with a small stability margin.

3. BREATHING DYNAMICS

The ISC in stoichiometric gasoline engines depends on the engine air flow control (or the engine air charge control) which is accomplished by directly controlling the intake valve duration, instead of indirectly controlling the intake manifold pressure through the electronic throttle (or air by-pass valve). The mean-value engine air flow for the camless engine is a function of the intake valve duration (IVD (deg)) and engine speed (N), i.e. $W_{\mathrm{e}}^{\mathrm{cml}} = F_{W_{\mathrm{e}}}^{\mathrm{cml}}(\mathrm{IVD}, N)$. In contrast to the camless unthrottled operation, the conventional throttled engine air flow (pumping rate) is a function of the intake manifold pressure (p_{m} (pa)) and the engine speed (N), i.e. $W_{\mathrm{e}}^{\mathrm{cnv}} = F_{W_{\mathrm{e}}}^{\mathrm{cnv}}(p_{\mathrm{m}}, N)$. The nonlinear static functions $F_{W_{\mathrm{e}}}^{\mathrm{cml}}$ [6] and $F_{W_{\mathrm{e}}}^{\mathrm{cnv}}$ [11] are shown as

$$\begin{aligned} W_{\mathrm{e}}^{\mathrm{cml}} &= F_{W_{\mathrm{e}}}^{\mathrm{cml}}(\mathrm{IVD}, N) \\ &= (7.37\times 10^{-16}N^2 + 3.15\times 10^{-12}N - 6.34\times 10^{-9})\times \mathrm{IVD}^2 \\ &\quad + (-1.92\times 10^{-13}N^2 - 5.94\times 10^{-10}N + 5.04\times 10^{-6})\times \mathrm{IVD} \\ &\quad + (6.75\times 10^{-12}N^2 + 1.43\times 10^{-8}N - 1.63\times 10^{-4}) \end{aligned} \tag{5}$$

$$\begin{aligned} W_{\mathrm{e}}^{\mathrm{cnv}} &= F_{W_{\mathrm{e}}}^{\mathrm{cnv}}(p_{\mathrm{m}}, N) \\ &= -\,6.18\times 10^{-5} - 1.91\times 10^{-6}N + (2.21\times 10^{-9} + 1.72\times 10^{-10}N)p_{\mathrm{m}} \end{aligned} \tag{6}$$

It is shown that the engine speed has the same effects in both conventional throttled and camless unthrottled engine pumping rates. In particular, a speed drop due to a torque disturbance will cause cylinder air flow to decrease which, if not corrected, can potentially cause a large transient. This is an internal feedback that exists in both throttled and unthrottled engines.

In the case of the conventional throttled engine, the dependency of pumping rate on manifold pressure creates another feedback loop that rejects the effect of engine speed on cylinder air flow. This is achieved through (i) the intake manifold filling dynamics that are modelled with the integrator shown in Figure 1, and (ii) the specific topology of the engine speed variations in the feedback loop [11]. Thus the self-regulating effects of the manifold filling dynamics reject the cylinder air flow variations before they propagate to the rotational dynamics, causing speed instability. Unfortunately, this is not the case with the camless unthrottled operation. Unthrottled conditions result in constant intake manifold pressure (approximately equal to atmospheric pressure) which eliminates the manifold filling dynamics. By loosing the pumping rate dependency on the manifold pressure we lose the self-regulating ability of the intake manifold filling dynamics. This difference is of central importance in the speed control problem because the self-regulating ability reduces the open-loop engine speed deviation in conventional throttled engines. We confirm this significance in Section 5 where we show that the linearized open-loop speed dynamics with the camless breathing $\Delta\mathrm{IVD} \to \Delta N$ has a stable pole very close to the imaginary axis, whereas the $\Delta\theta \to \Delta N$ open-loop dynamics in the conventional engine ($\Delta\theta$ is the air-bypass valve position or electronic throttle angle) are stable with poles far into the open left-half plane (OLHP). Reference to the absence of the self-regulating properties of the intake manifold dynamics can also be found in the experimental study by Urata *et al.* [8].

To make things worse, control of IVD is achieved through the hardware implementation of a signal v that is defined in the time domain and thus amplifies the speed to cylinder flow dependency. The next section describes this last piece of the camless engine dynamics that is responsible for the camless speed instability.

4. CAMLESS ACTUATION DYNAMICS

The majority of electro-hydraulic or electro-mechanical actuators used for camless valvetrain development are triggered in the time domain which has important implications in the engine dynamics. In this work, the camless actuation is achieved with an electro-hydraulic system introduced in Reference [3] and modelled in Reference [12]. The valve motion is controlled by a sequence of pulses generated by an electronic circuit. Figure 2 shows the intake valve profile (IVP) and its associated two pulses that trigger the opening, lift and closing of the valve. The valve opening and closing are triggered by t_{open} and t_{close}, respectively. From t_{open} to $t_{\text{open}} + \Delta t$, the valve moves with constant acceleration, hence, Δt controls the peak lift of the valve. By simplifying the trapezoidal valve profile with an ideal rectangular profile, it is clear that the intake valve duration is controlled by the difference in the pulse timing $v = t_{\text{close}} - t_{\text{open}} + \Delta t$. The cylinder air charge is more sensitive to the duration rather than the lift, especially, if the lift is above 3 mm [6]. For this reason, we choose IVD as the effective control signal of the camless breathing process.

From Figure 2, it is obvious that the degrees of IVD are controlled in the time domain by the time elapsed between the two pulses ($v = t_{\text{close}} - t_{\text{open}} + \Delta t$), which we call, with slight abuse of notation, the *pulse-interval*. The pulse-interval (v) is scheduled in the time domain. Therefore, the exact value of (crank-angle) degrees of IVD is a function of engine speed:

$$\begin{aligned}\text{IVD}(t) &= F_{\text{IVD}}((N(t), v(t - \tau_\alpha)) \\ &= 0.006N(t)v(t - \tau_\alpha) \qquad (7)\end{aligned}$$

where τ_α is the combination of sensing and controller–host computer communication delay. The initial experimental hardware indicates that a realistic scenario requires a delay equal to one cycle, i.e. $\tau_\alpha = 4\Delta T = 120/N$.

Equation (7) shows that if an increase in load causes a drop of 200 rpm in nominal engine speed and there is no adjustment to the valvetrain pulse-interval (open-loop system), then the demanded valve duration is reduced by 16.8°. For illustration we add Figure 3. The solid line shows the camless IVP for a 14 ms pulse-interval (input to the actuator) at 800 rpm, whereas the dashed line shows the valve profile that is generated by the same pulse-interval (14 ms) at 600 rpm. The

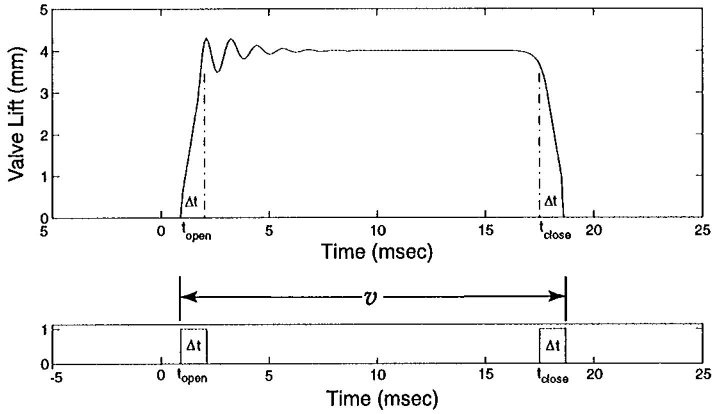

Figure 2. Intake valve profile generated by a pulse sequence.

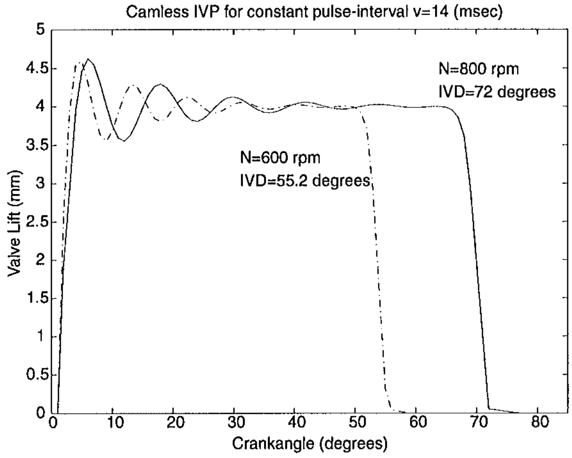

Figure 3. Intake valve profile for constant input pulse-interval ($v = 14\,\mathrm{ms}$) for 800 and 600 rpm.

decrease in intake valve duration results in a decrease in cylinder air flow, and consequently, a further decrease in engine speed. This relationship constitutes the second positive feedback loop inherent to the speed dynamics of a camless engine.

5. LINEARIZATION AND STABILITY ANALYSIS

The simple mathematical representation developed in the previous sections allows us here to demonstrate that the camless idle speed system is an unstable nonlinear system with considerable delays associated with the sensing/actuating interface and the discrete nature of the torque generation. Without downplaying the issues associated with the complex nonlinearities of the system [13], we are focusing on small-signal analysis and employ techniques pertinent to linear time invariant (LTI) systems. Linearization at a nominal point that corresponds to idle operation shows that the open-loop dynamics of the unthrottled camless engine have a right-half plane (RHP) pole and a significant time delay. To assess potential difficulties in the feedback controller design, we model the time delay as a non-minimum phase (NMP) zero using a first-order Padé approximation, and then in Section 6, apply well-known results on fundamental limitations for finite-dimensional LTI systems.

The state vector of the system is $x = [v_{\mathrm{del}}, m_{\mathrm{e}_{\mathrm{del}}}, N]'$, where $v_{\mathrm{del}}(t) = v(t - \tau_\alpha)$ is the delayed pulse-interval command, and $m_{\mathrm{e}_{\mathrm{del}}}(t) = m_{\mathrm{e}}(t - \tau_{\mathrm{e}})$ is the delayed (effective) engine air charge. The selection of a desired idle speed $N_0 = 800\,\mathrm{rpm}$, a nominal load torque $T_{q\mathrm{l}_0} = 0\,\mathrm{N\,m}$ and zero disturbance load $T_{q\mathrm{d}_0} = 0\,\mathrm{N\,m}$ defines the nominal operating point $P_0 = [x_0', v_0, T_{q\mathrm{l}_0}]'$. We introduce the following positive coefficients 'k_{xx}'.

$$k_N = \left.\frac{\partial T_{q\mathrm{f}}}{\partial N}\right| P_0$$

$$k_{q1} = \left.\frac{\partial T_{q\mathrm{e}}}{\partial m_{\mathrm{e}}}\right| P_0, \quad k_{q2} = \left.\frac{\partial T_{q\mathrm{e}}}{\partial N}\right| P_0$$

$$
\begin{aligned}
k_{m1} &= \frac{\partial m_e}{\partial W_e}\bigg|P_0, \quad k_{m2} = -\frac{\partial m_e}{\partial N}\bigg|P_0\\
k_{u1} &= \frac{\partial W_e}{\partial \mathrm{IVD}}\bigg|P_0, \quad k_{u2} = \frac{\partial W_e}{\partial N}\bigg|P_0\\
k_{v1} &= \frac{\partial \mathrm{IVD}}{\partial v}\bigg|P_0, \quad k_{v2} = \frac{\partial \mathrm{IVD}}{\partial N}\bigg|P_0
\end{aligned}
\tag{8}
$$

Figure 4 shows the block diagram of the linearized model using the positive constants above. From the linearized model, we obtain the transfer functions between pulse-interval, load torque and engine speed:

$$
\Delta N = \frac{k_{v1}k_{u1}k_{m1}k_{q1}\mathrm{e}^{-(\tau_\alpha+\tau_e)s}\Delta v - \Delta T_{qd}}{[Js + (k_N - k_{q2})] - [(k_{v2}k_{u1} + k_{u2})k_{m1} - k_{m2}]k_{q1}\mathrm{e}^{-\tau_e s}}
\tag{9}
$$

Substitution of all of the numerical values of the coefficients obtained at the nominal operating point and using first-order Padé approximation $\mathrm{e}^{-\tau s} = (1 - \frac{1}{2}\tau s)/(1 + \frac{1}{2}\tau s)$ result in two real roots. One root lies in the OLHP (henceforth called p_s) and another one lies in the ORHP (henceforth called p_u). We denote $-2/(\tau_\alpha + \tau_e)$ as p_τ, which is the pole from the Padé approximation and is also stable. In the following transfer function, we also denote as $z_s = -2/\tau_e$ and $z_u = 2/(\tau_e + \tau_\alpha)$ the minimum- and non-minimum-phase zeros from the Padé approximation

$$
\begin{aligned}
\Delta N &= G_3(G_2G_1\Delta v - \Delta T_{qd}), \quad \text{where}\\
G_1 &= -\frac{(s - z_u)}{(s - p_\tau)}\\
G_2 &= k_{v1}k_{u1}k_{m1}k_{q1}\\
G_3 &= \frac{s - z_s}{J(s - p_s)(s - p_u)}
\end{aligned}
\tag{10}
$$

The linearized plant is used to investigate the stability of the open-loop dynamics. This analysis, which progresses from right to left by breaking the feedback loop at lines 1–3 in the model of Figure 4, clarifies the source of the instability in the camless engine speed dynamics, i.e. which variable and which interconnection contribute to the ORHP pole. The transfer functions

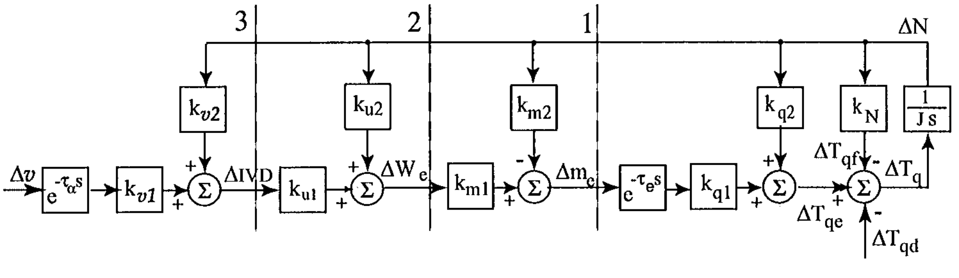

Figure 4. Linearized model of the camless unthrottled engine.

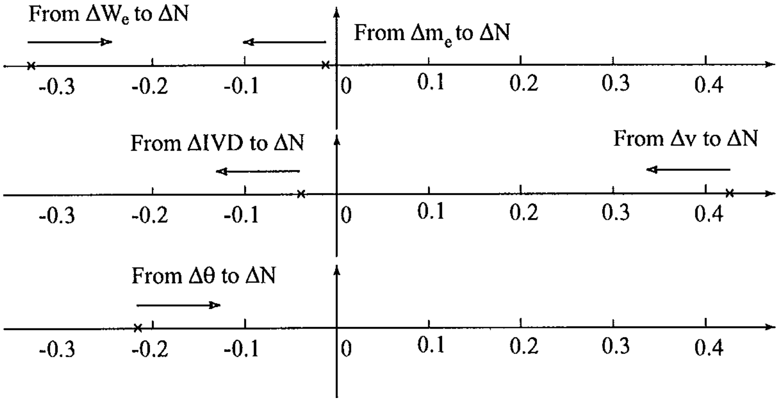

Figure 5. Relation between the dominant poles and the nominal engine speed in the s-plane. The top two graphs refer to the pole of the camless system, and the lowest graph refers to the pole of a conventional system.

from ΔIVD to ΔN, ΔW_e to ΔN, and Δm_e to ΔN, or the transfer functions to the right of the lines 1, 2 and 3 in Figure 4, have dominant poles at -0.04, -0.33 and -0.01, respectively. Although these dominant poles are all in the LHP, the first and the third are very close to the origin. For comparison, the dominant pole from $\Delta\theta$ to ΔN in the same displacement conventional (throttled with mechanical valvetrain) engine is -0.22. Figure 5 shows the location of these dominant poles, and the arrows show the change of their location as the nominal idle engine speed increases. Note that when the nominal engine speed increases, the camless speed dynamics become more stable. It is found that the system becomes stable at nominal load torque $T_{qd0} = 0\,\mathrm{N\,m}$ and nominal speed $N_0 = 1700\,\mathrm{rpm}$.

Since the ISC problem is a speed regulation problem, we do not consider the variation of the nominal engine speed $N_0 = 800\,\mathrm{rpm}$. We do consider, however, the effects of non-zero load torque (heater or rear window defroster on, for example) on the plant dynamics. Another important source of model uncertainty is the variation of the inertia J in (10) during vehicle launch. We consider the values of J to be in the following range:

$$J \in [0.25, 0.37]\,\mathrm{kg\,m^2} \tag{11}$$

while the load torque is in the following range:

$$T_{ql} \in [0, 50]\,\mathrm{Nm} \tag{12}$$

Figure 6 shows the effects of inertia and load torque on the plant gain, stable (p_s) and unstable poles (p_u) in (10).

It is found from the figure above that when the load torque increases and/or inertia decreases, the unstable pole is moving further from the origin, and thus becoming more unstable. Therefore, when the load torque is minimum and inertial is maximum in their ranges, we will have the most stable plant, and we call it the 'best case' plant. Similarly, we define as the 'worst case' plant the one that corresponds to the maximum load torque and the minimum inertia possible.

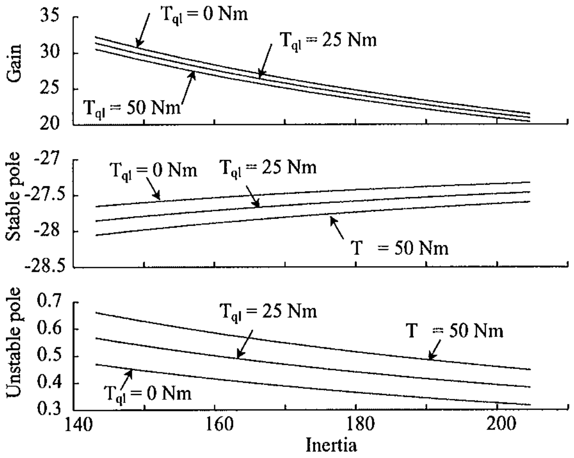

Figure 6. Variations in gain, stable and unstable poles for varying inertia and load torque.

6. FEEDBACK LIMITATIONS

Analysis of the relative pole and zero locations can be used to assess the inherent system limitations for a wide class of causal, stable and linear stabilizing controllers. The existence of unstable open-loop dynamics and delays in the feedback-loop imposes well-known constraints in the closed-loop performance. Identifying these constraints for the nominal engine provides guidelines for the controller design in Section 8.2.

Let us consider the unity SISO feedback system with a linear, causal and stable controller $C(s)$ as shown in Figure 7, where ΔN is the engine speed variation (performance and measurement), Δv is the pulse-interval variation, ΔT_{qd} is the torque load variation. Following the conventional notation for disturbance rejection problems we have $G = G_3 G_2 G_1$. Let $L(s) = G(s)C(s)$ be the open-loop transfer function, $S(s) = 1/(1 + L(s))$ the sensitivity function and $T(s) = L(s)/(1 + L(s))$ the complementary sensitivity function.

As mentioned previously, linearization of the camless engine model at nominal engine speed $N_0 = 800\,\mathrm{rpm}$ and load torque $T_{qd0} = 0$ results in an RHP pole $p_u = 0.47$ and an NMP zero $z_u = 8.9$. Their relative locations ($z_u \approx 19 p_u$) are not restrictive if one adheres to the 'rule of thumb' that the open-loop crossover frequency (ω_c) should be $2p_u \leqslant \omega_c \leqslant z_u/2$ (see References [14–16]). Using a stable controller on the nominal plant allows us to calculate bounds such as the sensitivity peak $M_S \geqslant (z_u + p_u)/(z_u - p_u)$ [16] to have a minimum of $M_S \geqslant 1.04$. Similarly, the integral constraints associated with the existence of an RHP pole and the NMP zero do not pose any additional difficulties. The same conclusion holds even if we consider the more restrictive phase limitations of the delay [17] instead of optimistically approximating the delay with an NMP zero.

On the other hand, a brief calculation of the pole-zero location for a vehicle with smaller inertia indicates a difficult feedback problem with $z_u \approx 3.3 p_u$. Similar difficulties were found for operation under heavy load. Even though, these 'difficult' cases are application specific, they indicate the need for a comprehensive study of the relative pole and delay values in order to assess the system's feasibility.

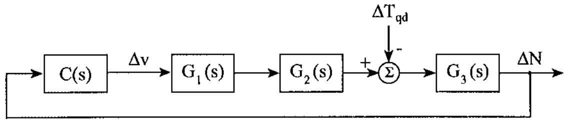

Figure 7. Unity feedback control system for the camless unthrottled engine.

The well-known result $2p_u \leqslant \omega_c \leqslant z_u/2$ used in the nominal case above indicates that a stable controller exists, but it does not guarantee that the achieved closed-loop performance and robustness will be acceptable for the stringent idle speed control requirements. Further investigation is required using realistic bounds on sensitivity that reflect desired specifications on the disturbance rejection of the ISC. Examples of such bounds can be found in Reference [18], or one can interpret time-domain specifications found in Reference [9]. Specifically, a typical test for the ISC problem consists of a 15 N m (unmeasured) torque disturbance and a desired disturbance rejection bandwidth of $\omega_c^* = 10$ rad/s. This bandwidth cannot be accomplished with a stable controller in the case of the camless engine because $\omega_c^* > z_u$. Note here that an unstable controller is undesirable due to associated implementation difficulties. Moreover, the bound on the sensitivity peak M_S we calculated above will increase due to the additional unstable pole in $L(s)$. For comparison, consider the conventional engine at idle conditions. The location of RHP-zero is at $z_{\text{conv}} = 2(1/\Delta T) \approx 26.7$. Obviously, the small delay in the conventional feedback allows $\omega_c \leqslant 13.3$ rad/s, which implies faster disturbance rejection than is currently feasible for the camless operation ($\omega_c \leqslant 8.9$) rad/s.

Even less stringent performance requirements introduce poor sensitivity properties. Consider a bound on the sensitivity function modelled by $W_p(s) = (s/M_S + \omega_B^*)/s$, where the minimum desired bandwidth is $\omega_B^* = 4.5$ rad/s (ω_B^* is the frequency where the straight-line approximation of W_p is equal to 1) and M_S is the sensitivity peak. Using the interpolation constraint $S(z_u) = 1$ that the NMP zero introduces, we conclude that

$$|W_p(z)| = |W_p(z)S(z)| \leqslant \|W_pS\|_\infty \leqslant 1 \tag{13}$$

The last inequality reflects the performance specification $\|W_pS\|_\infty < 1$. Solving (13) for M_S suggests that the closed-loop system might have unacceptable robustness properties in intermediate frequencies, because there, $M_S \geqslant 2$.

From the above analysis it is clear that the long (one cycle) delay due to the controller/hardware interface limits the closed-loop performance. The interpolation constraint associated with the unstable pole ($T(p_u) = 1$) does not point to any additional difficulties, other than the need for a stabilizing controller ($T(p_u) = 1 \Rightarrow \|T\|_\infty \geqslant 1$ which requires $C(s) \neq 0$).

7. UNCERTAINTY MODELLING

Apart from the limitations in the nominal performance, model uncertainty and parameter variations impose more difficulties in the controller design. Analysis and modelling of the system uncertainty are presented in this section. For simplicity, the open-loop speed equation is rewritten as

$$\Delta N = k\left[\frac{s - z_s}{J(s^2 + as - b)}\right]e^{-(\tau_e + \tau_x)s}\Delta v - \left[\frac{s - z_s}{J(s^2 + as - b)}\right]\Delta T_{qd} \tag{14}$$

where $k = G_2$ is defined in (10) and G_3 is rewritten from (10) as $(s - z_s)/J(s^2 + as - b)$, where $a = -(p_s + p_u)$ and $b = -p_s p_u$.

The inertia J varies in the range shown in (11). The value of the load torque also varies as shown in (12).

It is found that when the load torque increases, k decreases, a increases and b increases, all monotonically. When the inertia increases, k does not change, while both a and b decrease monotonically. When the load is 0 N m and the inertia is 0.37 kg m^2, the linearization results in the smallest RHP pole (best case scenario) and the values of k, a and b are

$$k = 7.93, \quad a = 27.01, \quad b = 8.66 \tag{15}$$

When the load is 50 N m and the inertia is 0.25 kg m^2 (largest RHP pole or worst case scenario), we get the following values:

$$k = 7.52, \quad a = 27.39, \quad b = 18.55 \tag{16}$$

When the load is between 0 and 50 N m, and the inertia is between 0.25 and 0.37 kg m^2, k, a and b take values in the range shown in (15) and (16).

Based on the parameter variation, it is straightforward to choose the nominal model as the one that corresponds to the average values of k, a, b, J ($k_0 = 7.72$, $a_0 = 27.20$, $b_0 = 13.61$, $J_0 = 0.31$, respectively). The plants with parameters k, a and b which are in the range shown in (15) and (16) correspond to the perturbed models.

The disturbance transfer function G_3 depends on the load torque and the inertia. The gain G_2 depends on the load torque only. Since the variations of the load torque and the inertia are independent, we can model these uncertainties part by part. In particular, we consider a multiplicative uncertainty structure to model the uncertainty in G_2 and G_3, where $G_{Pi} = G_i(I + W_i\Delta_i)$ is the form of multiplicative uncertainty. G_{Pi} and G_i for $i = 2, 3$ are the perturbed and nominal plant. Therefore we get $|W_i(j\omega)\Delta_i(j\omega)| = [|G_{Pi}(j\omega) - G_i(j\omega)|]/|G_i(j\omega)|$, where $|G_{Pi}(j\omega) - G_i(j\omega)|$ is the distance between the perturbed plant and the nominal plant at frequency ω.

The uncertainty in the gain G_2 is easily modelled with multiplicative uncertainty. We have $G_{P2} \in [7.52, 7.93]$, $G_2 = 7.72$, so using the multiplicative notation we have $G_{P2} = G_2(1 + W_2\Delta_2)$, where $W_2 = 2.65 \times 10^{-2}$, $\Delta_2 = \delta$ and $\delta \in [-1, 1]$.

The multiplicative uncertainty model of the disturbance transfer function G_3 is directly obtained using the Nyquist plots of G_{P3}. Figure 8 shows G_3 (solid line) and G_{P3} (*) at two different frequencies. It also shows how the load torque and inertia change the perturbed plant at these frequencies.

We use a circle to cover all the uncertainty at each frequency with a radius $R_3(\omega)$. We have that $|G_{P3}(j\omega) - G_3(j\omega)| \leqslant R_3(\omega)$, and consequently $|W_3(j\omega)\Delta_3(j\omega)| \leqslant R_3(\omega)/|G_3(j\omega)|$. Figure 9 shows $R_3(\omega)/|G_3(j\omega)|$ and the gain of a first-order function $W_3(s) = (0.25s + 0.10)/(s + 0.47)$, which ensures that $R_3(\omega)/|G_3(j\omega)| \leqslant |W_3(j\omega)|$. Therefore, we have a perturbed plant of G_{P3} as $G_{P3} = G_3(1 + W_3\Delta_3)$, where W_3 is shown above and Δ_3 satisfies $|\Delta_3| \leqslant 1$. Note that by choosing

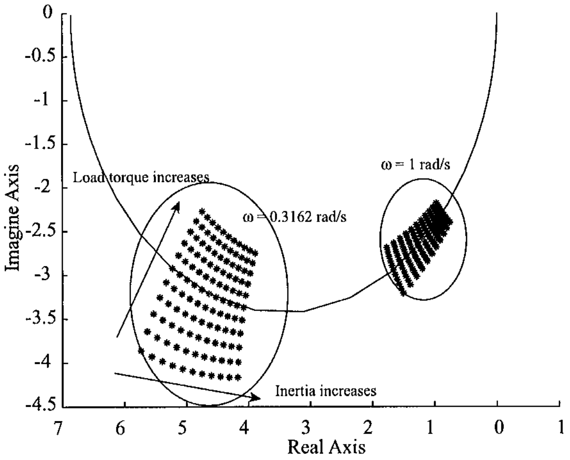

Figure 8. The Nyquist plots of the disturbance transfer function G_3 (solid line) with perturbation G_{P3} (*).

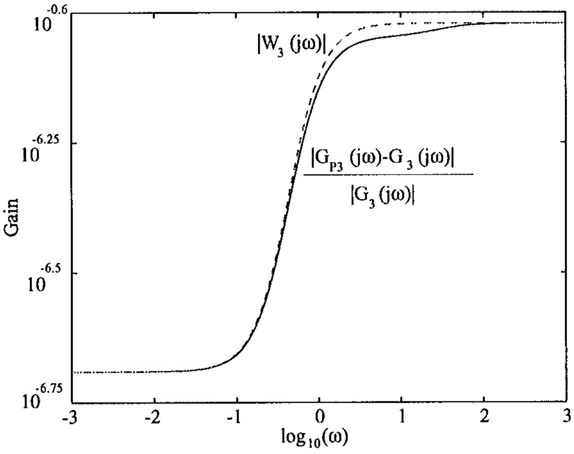

Figure 9. The upper bound of the multiplicative uncertainty gain in $G_2(j\omega)$.

$W_3(s)$ as the above weight function, we have a perturbed disturbance gain slightly more conservative than the actual perturbation.

8. CAMLESS ISC CONTROLLER DESIGN

A robustly stabilizing PI controller and two high-order robust controller designs based on H_∞ and μ synthesis are designed here.

8.1. PI controller design

For the PI controller design $C(s) = k_P + k_I/s$, the root locus method is applied to determine the combination of k_P and K_I that can stabilize the plant for the range of inertia and load torque defined in (11) and (12). Figures 10 and 11 show the resulting k_P and k_I values. The region for the allowable values is encircled by the curves and x-axis. It is shown that a change in load torque shifts the region along the x-axis, while the decrease of inertia reduces significantly the allowable region.

It is found that a set of k_P and k_I values can be chosen that stabilize the plant under any possible variation of inertia and load. In this region, $k_P = 0.13$ and $k_I = 0.12$ are chosen for achieving fast closed-loop response and large damping. Figure 12 shows the step response to a 1 N m disturbance for the worst, nominal and best cases. As expected, it is found that the response of the best case has the smallest speed excursion and oscillation.

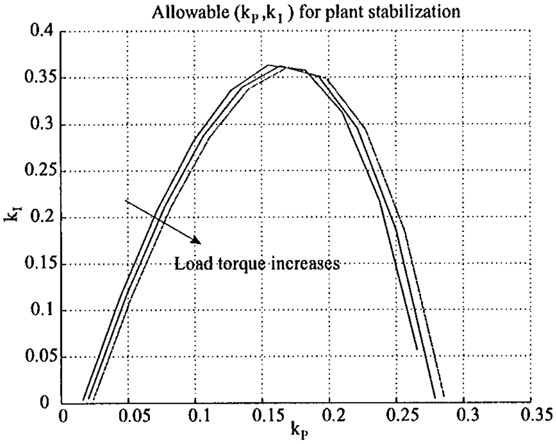

Figure 10. Region of k_P and k_I values for different load values.

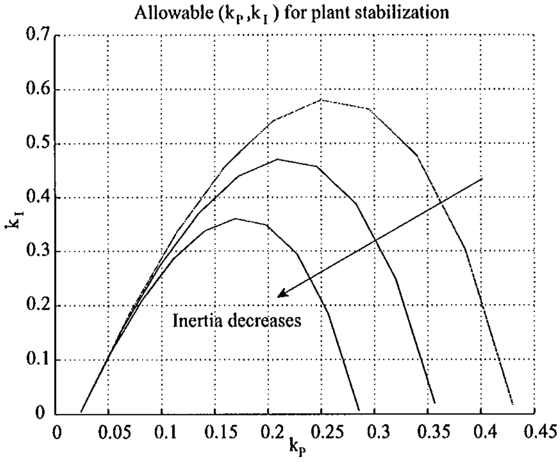

Figure 11. Region of k_P and k_I values for different inertia values.

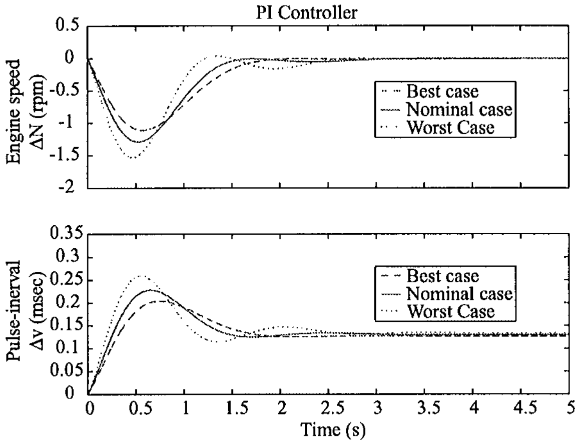

Figure 12. Step response to 1 N m disturbance for worst, nominal and best case plant.

8.2. Robust controller design

The PI controller design is only a first-order controller and cannot directly address requirements on nominal performance-loop shaping and robust performance. In this section, H_∞ [19] and μ [20] synthesis are used to design higher-order controllers based on the uncertainty model in Section 7.

The block diagram of the perturbed model with the standard input/output representation is shown in Figure 13. The perturbed plant is already discussed in Section 7. The selection of the performance weight, W_p, is based on the limitation analysis, where we showed that a closed-loop bandwidth of 4.5 rad/s will result in a sensitivity peak of 2. The performance weight $W_p = (s/B + \omega_B^*)/(s + \omega_B^*/A)$ is chosen with $B = 2$ so that there is good high-frequency disturbance rejection, the allowable steady-state error is less than the *DC* gain $1/A = 0.01$, and the minimum bandwidth is $\omega_B^* = 1.5$ rad/s in order to achieve good disturbance response in the nonlinear simulations (in Figure 19) that follow. The noise weight, W_n, is chosen with bandwidth 500 rad/s and the noise mean value of 0.008 rpm based on typical wheel speed sensor characteristics. The control action weight $W_c = 1$ was chosen.

Figure 14 shows the robust stability, nominal performance and robust performance plots for the H_∞ and μ controller. Both controllers ensure robust stability. The μ controller sacrifices some of the nominal performance in order to achieve robust performance. The step disturbance (1 N m) responses of the closed-loop system with these two controllers are shown in Figures 15 and 16. It is found that the H_∞ controller results in larger closed-loop bandwidth, while the μ-based closed loop has smaller speed excursion.

For comparison, Figure 17 shows the magnitude of the three controllers, namely *PI*, H_∞ and μ. Both H_∞ and μ show high-frequency content which imposes stringent requirements on their digital implementation.

Figure 18 shows the Nyquist plots of the closed-loop system with these three controllers. It shows that the H_∞ and μ controllers exploit the high frequencies, as long as the uncertainty and the noise are small, and boost the gain once they have brought the loop around the 1 point. Note here that we analysed the positive feedback system, thus stability is defined by the $1 + j_0$ point.

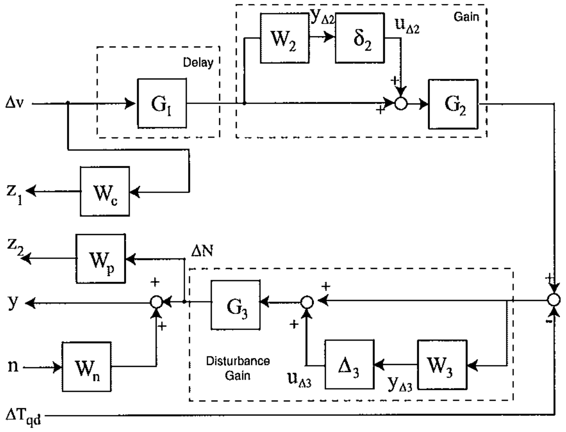

Figure 13. Block diagram of the perturbed system.

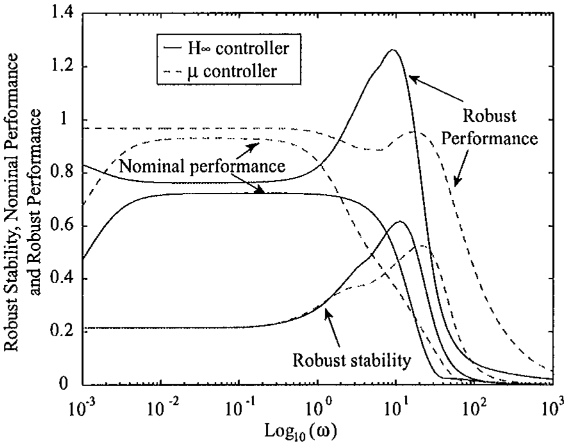

Figure 14. Robust stability, nominal performance and robust performance plot of closed loop with an H_∞ and μ controllers.

The gain at high frequencies is further increased to force a fast roll-off based on the closed-loop analytical constraint.

Finally, Figure 19 shows the 15 N m disturbance response of the closed-loop nominal nonlinear system with *PI*, H_∞ and μ controllers. Both the H_∞ and μ controllers outperform the *PI*, but still have longer transient response time than that of conventional engines [9]. Table I shows the transient time and maximum deviation of the speed for the closed-loop nonlinear system with the *PI*, H_∞ and μ controllers during disturbance torque of 15, 20 and 25 N m.

9. CONCLUDING REMARKS

In this paper, we formulated the idle speed control problem for a SI engine equipped with a camless electro-hydraulic valvetrain. We showed that unthrottled camless operation results in

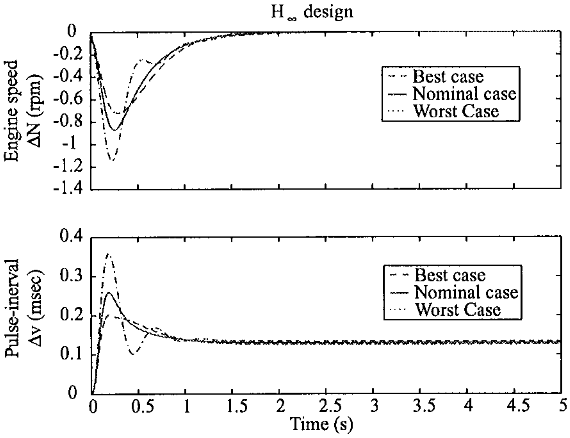

Figure 15. Step disturbance response and control effort disturbance response plot of closed loop with an H_∞ controller.

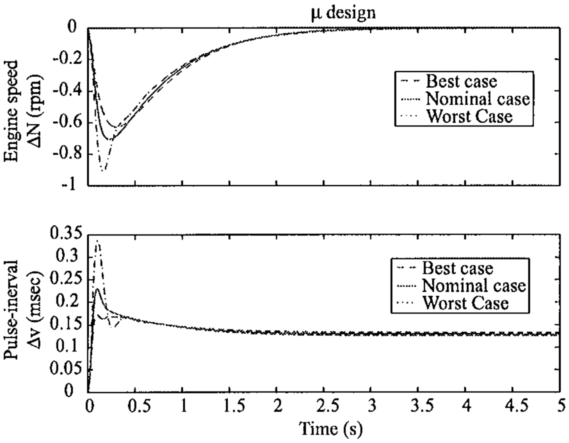

Figure 16. Step disturbance response and control effort disturbance response plot of closed loop with a μ controller.

unstable open-loop dynamics at idle. We demonstrated using linear theoretic techniques that the unstable pole and controller/hardware delay impose limitations in the achievable disturbance rejection performance of the closed-loop system. The effects and benefits of spark timing as an additional control variable for the ISC problem will be investigated in future work.

It is important to mention that analysis in the continuous crank-angle domain does not change the stability results presented here. Analysis in the crank-angle domain scales the location of poles and zeros by a positive number, i.e. does not change their relative ratio and their unstable–stable characteristics [21, 22]. Thus, the fundamental limits associated with the RHP pole and NMP zero remain as studied here. Analysis in the crank-angle domain might facilitate the robust

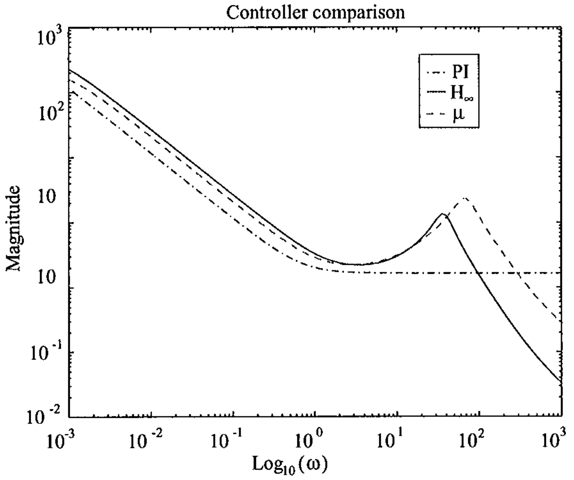

Figure 17. Magnitude plots of the *PI*, H_∞ and μ controllers.

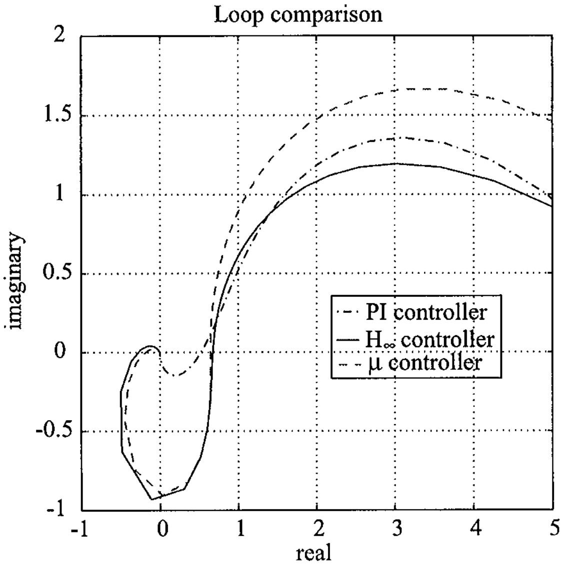

Figure 18. Nyquist plots of closed loop system with the *PI*, H_∞ and μ controllers.

control design because the plant parameter variations with respect to engine speed are smaller than the variations observed in the time-domain analysis.

Our analysis on the relative pole/zero locations can help future decision about the minimum idle speed, the maximum vehicle inertia and the computational resources in camless engine-powered vehicles. The system instability, coupled with potentially large delay, requires a detailed

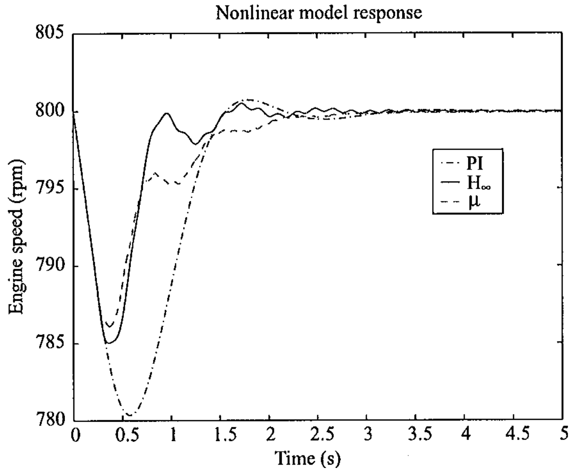

Figure 19. Response of the closed-loop nonlinear system with the *PI*, H_∞ and μ controllers during a 15 N m disturbance torque.

Table I

	Maximum speed deviation (rpm)/Transient response time (s)		
Disturbance load (N m)	PI	H_∞	μ
15	18/2.58	15/1.48	14/1.90
20	24/3.44	20/1.49	18/1.96
25	30/3.58	25/1.50	22/2.00

analysis and formal ways of testing software interrupts and priorities among tasks. Although non-trivial, these implementation issues have been successfully addressed in the production of diesel fuel governors and injection systems. Advances in real-time computing and controller hardware are expected to significantly reduce this delay in the near future, making camless technology a potential candidate for the new generation of highly efficient vehicles.

APPENDIX A: NOMENCLATURE

J	total rotational inertia (kg m^2)
N	engine Speed (rpm)
$T_{q\mathrm{e}}$	net torque generated by combustion (N m)
$T_{q\mathrm{f}}$	torque due to mechanical friction and other losses (N m)
$T_{q\mathrm{d}}$	disturbance torque (N m)
$T_{q\mathrm{l}}$	load torque (N m)
m_e	engine air charge (kg)
τ_e	induction-to-power delay (s)

ΔT	stroke event (s)
W_{e}	mean-value engine air flow (kg/s)
IVD	intake valve duration (deg)
v	pulse-interval (s)
τ_{α}	sensing and computational delay (s)
θ	throttle angle (deg)
$\dot{m}_{\theta}$	air flow into the manifold (kg/s)

ACKNOWLEDGEMENTS

Support is provided by the National Science Foundation under contracts ECS-00-49025 (Stefanopoulou) and ECS-99-78562 (Smith); matching funds to these grants were provided by Ford Motor Company.

REFERENCES

1. Ahmad T, Theobald MA. A survey of variable valve actuation technology. *SAE* 891674.
2. Gray C. A review of variable engine valve timing. *SAE* 880386.
3. Schechter MM, Levin MB. Camless engine. *SAE* 960581.
4. Elrod AC, Nelson MT. Development of a variable valve timing engine to eliminate the pumping losses associated with throttled operation. *SAE* 860537.
5. Miller RH *et al.* Unthrottled camless valvetrain strategy for spark-ignited engines. *Proceedings of the 19th ASME Conference*, ICE-Vol. 29-1, 1997; 81–94.
6. Ashhab MS, Stefanopoulou AG, Cook JA, Levin MB. Control-oriented model for camless intake process (Part I). *ASME Journal of Dynamic Systems, Measurement, and Control*, 2000; **122**:122–130.
7. Sono H, Umiyama H. A study of combustion stability of non-throttling SI engine with early intake valve closing mechanism. *SAE* 945009.
8. Urata Y, Umiyama H, Shimizu K, Fujiyoshi Y, Sono H, Fukuo K. A study of vehicle equipped with non throttling SI engine with early intake valve closing. *SAE* 930820.
9. Hrovat D, Sun J. Models and control methodologies for IC engine idle speed control design. *Control Engineering Practice* 1997; **5**(8):1093–1100.
10. Guzzella L, Amstutz A. Control of diesel engines. *IEEE Control Systems Magazine* 1998; **18**(5):53–71.
11. Stefanopoulou AG, Cook JA, Grizzle JW, Freudenberg JS. Joint air–fuel ratio and torque regulation using secondary cylinder air flow actuators. *ASME Journal of Dynamic Systems, Measurement, and Control* 1999; **121**(4):638–647.
12. Kim D, Anderson M, Tsao TC, Levin MB. A dynamic model of a springless electrohydraulic camless valvetrain system. *SAE* 970248.
13. Kang JM, Grizzle JW. Dynamic control of a SI engine with variable intake valve timing. *IEEE Transactions on Control System Technology*.
14. Freudenberg JS, Looze DP. Right half plane poles and zeros and design tradeoffs in feedback systems. *IEEE Transactions on Automatic Control* 1995; **AC-30**(6):555–565.
15. Seron MM, Braslavsky JH, Goodwin GC. *Fundamental Limitations in Filtering and Control.* Spinger–Berlin, 1997.
16. Skogestad S, Postlethwaite I. *Multivariable Feedback Control: Analysis and Design.* Wiley: New York, 1996.
17. Looze DP, Freudenberg JS. Limitations of feedback properties imposed by open-loop right half plane poles. *IEEE Transactions on Automatic Control* 1991; **36**(6):736–739.
18. Williams SJ, Hrovat D, Davey C, Maclay D, Crevel JW, Chen LF. Idle speed control design using an H_{∞} approach. *Proceedings of the ACC*, 1989; 1950–1956.
19. Chin YK, Coats FE. Engine dynamics: time-based versus crank-angle based. *SAE* 860412.
20. Yurkovich S, Simpson M. Crank-angle domain modeling and control for idle speed. *SAE* 970027.
21. Doyle JC, Glover K, Khargonekar P, Francis B. State-space solutions to standard H_2 and H_{∞} control problems. *IEEE Transactions on Automatic Control* 1989; **AC-34**(8):831–847.
22. Balas CJ, Doyle JC, Glover K, Packard K, Smith R. μ-Analysis and synthesis toolbox. *Matlab Manual* 1998.